
Detecting SZ Clusters Using Pixons

Vincent Eke

Steward Observatory, 933 N Cherry Ave, Tucson, AZ 85721, USA

Abstract. A speedy pixon algorithm for image reconstruction is described. The application of the method to a simulated Planck data set is also reported. This focusses on the extraction of galaxy clusters from multiwavelength microwave sky maps using the spectral dependence of the Sunyaev-Zel'dovich effect to distinguish them from the microwave background fluctuations and the instrumental noise. The ability of the technique to detect real sources in low signal-to-noise data is demonstrated.

1 Introduction

The pixon image reconstruction method is an iterative non-linear algorithm to infer a true underlying image, \hat{T} , given a measured data image

$$D(\mathbf{x}) = (T * B)(\mathbf{x}) + N(\mathbf{x}), \quad (1)$$

where \mathbf{x} represents a pixel position, T is the true image, B is the point-spread function (psf) of the measuring instrument, assumed to be invariant across the image, N is the associated statistical noise and $*$ represents the convolution operator.

In addition to requiring that the residual field is statistically indistinguishable from the anticipated noise, the pixon method reduces the acceptable solution space by favouring the simplest \hat{T} over those with more degrees of freedom that also provide an acceptable fit. Operationally, the simplicity is reduced by describing the inferred truth in a pixon, rather than pixel, basis. These pixons are collections of pixels with various sizes, chosen such that the amount of information is the same in each pixon. This leads to a smooth inferred truth where the data is insufficient to merit more degrees of freedom in the reconstruction, and small pixons in parts of the image where a lot of information per pixel existed.

This approach to image reconstruction was introduced by Piña & Puetter [1], and has been applied to a variety of astronomical data sets (e.g. [2], [3], [4], [5] and [6]). A detailed discussion of the theoretical basis of the pixon, as well as a list of applications of the method can be found in [7].

The speedy pixon algorithm is an iterative method that changes the number of pixons being used to describe the inferred truth until it uses the fewest pixons that allow a good fit to the data. Each change of the distribution of pixon sizes is followed by a conjugate gradient maximisation of the likelihood

(or equivalently minimisation of the misfit statistic) for the fixed pixion distribution. A flow diagram outlining the entire procedure is shown in Figure 1, and a fuller description of the algorithm is given in [8].

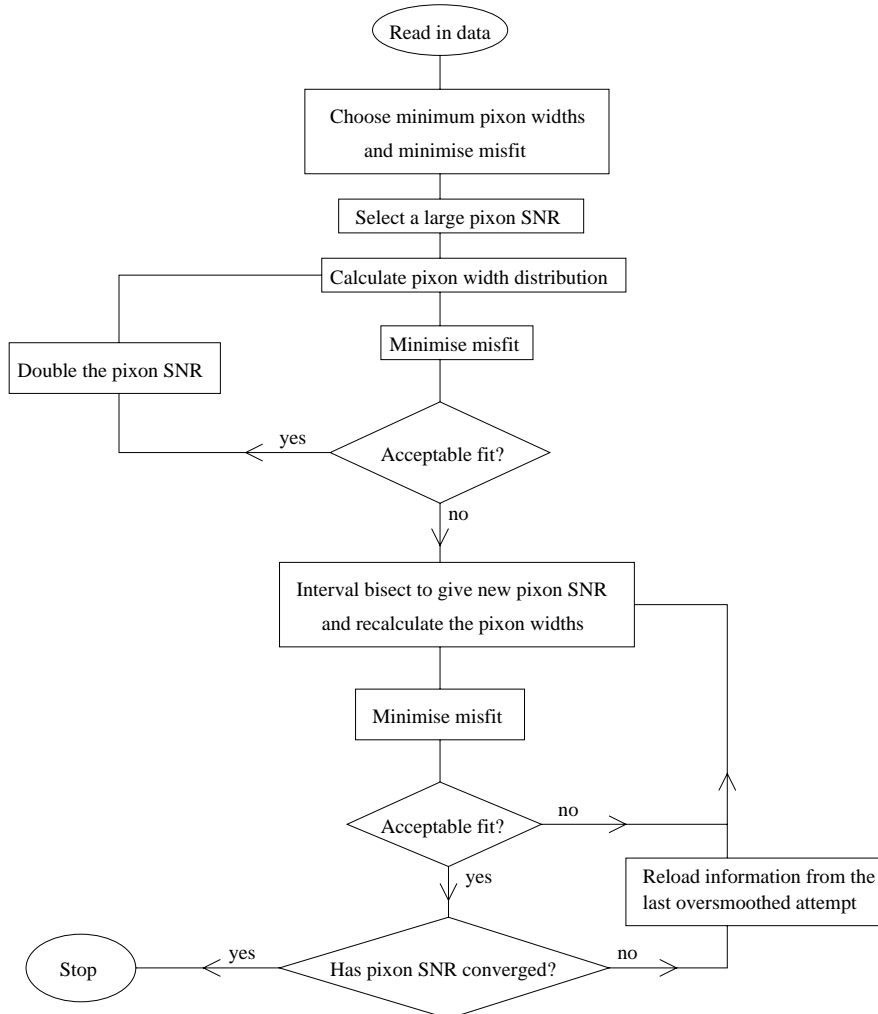


Fig. 1. Flow diagram showing the structure of the algorithm. There is an initial maximum likelihood type of fit, with all pixion widths taking the minimum available value. The resulting pseudoimage is used to find a pixion SNR that is too large to enable an acceptable fit to be found. Then the largest pixion SNR giving rise to an acceptable residual distribution is found by interval bisection

2 Multiwavelength Cluster Detection in Simulated CMB Data

The Planck surveyor satellite [9] is expected to return maps of the sky in a number of microwave wavelength ranges. In addition to the intrinsic CMB fluctuations, a number of interesting foregrounds will also contribute to these maps. One such contribution will come from the Sunyaev-Zel'dovich (SZ) effect produced when CMB photons are inverse Compton scattered during their passage through the ionised gas in galaxy clusters [10]. The distinctive spectral distortion created by the net heating of CMB photons in the directions of galaxy clusters should enable some thousands of clusters to be detected by Planck [11].

Table 1. Lists of (1) the central Planck observing frequencies employed here (GHz); (2) the Gaussian full width half maxima (arcmin); (3) the 1σ Gaussian noise per 1.5 arcmin square pixel in mJy (for 14 months of observations); (4) the conversion factor relating thermodynamic CMB $\Delta T/T$, in units of 10^{-6} , to the change in flux in mJy in a pixel; (5) the conversion factor relating the Comptonisation parameter y , in units of 10^{-6} , to the change in flux in mJy in a pixel; (6) the rms cluster $T * B$ per pixel (mJy); (7) the rms intrinsic CMB $T * B$ per pixel (mJy).

(1)	(2)	(3)	(4)	(5)	(6)	(7)
Frequency	fwhm	Noise	$\omega_{SZ}(j)$	$\omega_{CMB}(j)$	rms $T_{SZ} * B$	rms $T_{CMB} * B$
100	10.7	1.2	-0.19	0.124	0.20	4.6
143	8.0	2.2	-0.20	0.197	0.23	7.6
217	5.5	3.1	-1.9×10^{-3}	0.249	2.3×10^{-3}	9.9
353	5.0	5.8	0.34	0.155	0.43	6.2

Data Production A 400^2 pixel, 10 degree square field of simulated CMB sky, was created including both intrinsic CMB fluctuations and thermal SZ distortions produced by clusters. The intrinsic CMB map was a realisation of the standard Cold Dark Matter model using the power spectrum returned by CMBFAST [12]. The thermal SZ map was produced by creating some templates from hydrodynamical galaxy cluster simulations [13] and then pasting these, suitably scaled, at random angular positions with mass and redshift distributions according to the Press-Schechter formalism [14]. The thermal SZ Comptonization parameter, y , and the thermodynamic $\Delta T/T$ of the intrinsic CMB fluctuations were converted to fluxes per pixel in mJy in each of four wavebands by multiplying by $\omega_c(j)$ as listed in columns 4 and 5 of Table 1. These four combined truths were then ‘observed’ by applying the relevant Gaussian beam and adding the pixel noise appropriate to each wavelength (see columns 2 and 3 of Table 1).

The final two columns in Table 1 show the rms $T_c * B$ per pixel produced by each of the two components separately. These numbers demonstrate both

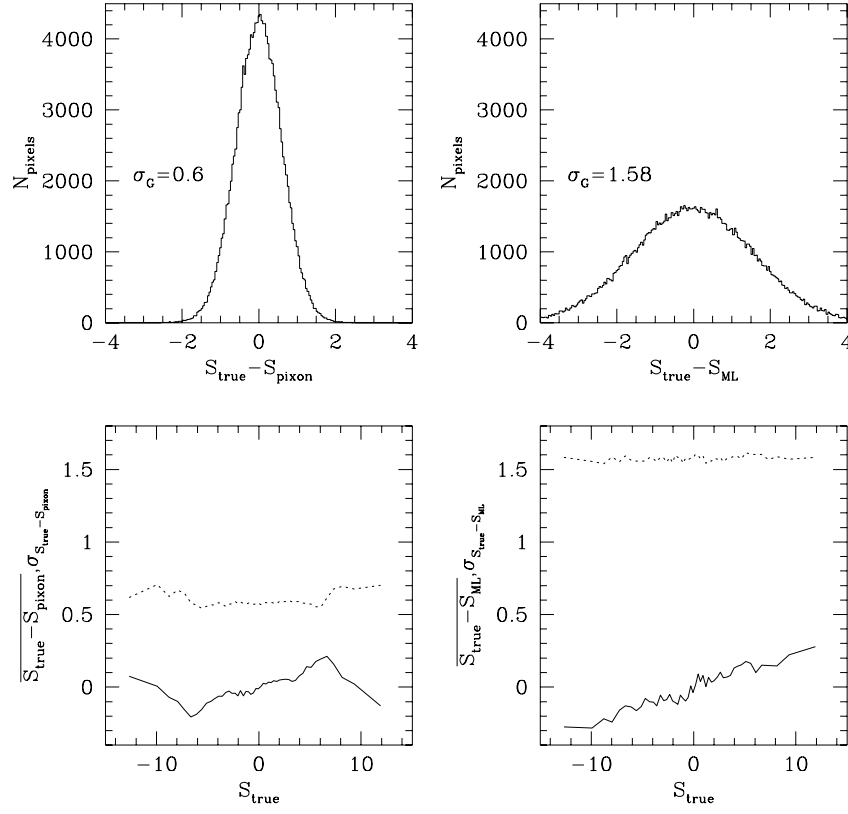


Fig. 2. The top left panel contains a histogram of the difference between the true and pixon-inferred intrinsic CMB component fluxes at 100 GHz in each pixel. Flux units are mJy for all panels in this figure. The width of the best-fitting Gaussian is also given. In the lower left panel, the solid line represents the average difference between the true and pixon-inferred intrinsic CMB component fluxes as a function of the true pixel flux, and the dotted line traces the standard deviation of the reconstruction error. The two right hand panels show the corresponding results for the ML reconstruction. In both cases, the Gaussian fits to the reconstruction errors are not shown because they essentially lie on top of the histograms

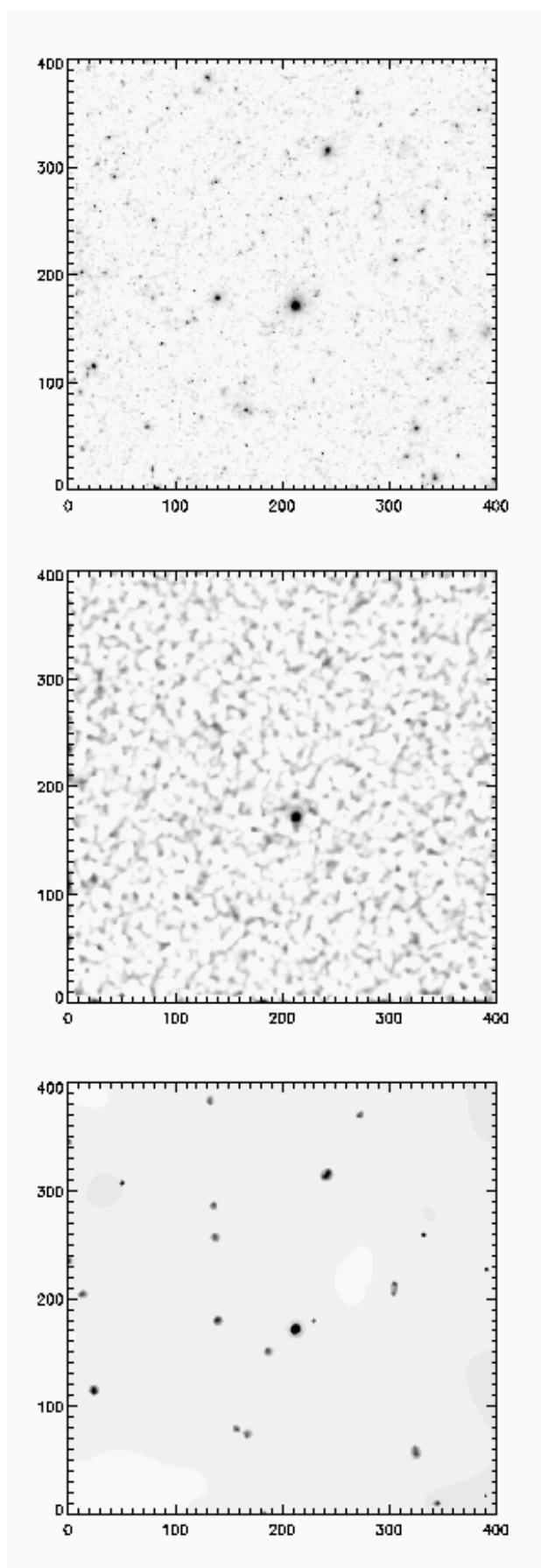


Fig. 3. The true thermal SZ y map is shown in the top panel, and the ML and pixon-inferred truths are contained in the second and third panels respectively. Axes are labelled in pixels

the high SNR with which Planck will observe the intrinsic CMB fluctuations and the relatively low SNR of the SZ clusters in the field, after convolution with the instrumental psfs.

Results In Figure 2, the pixon and ML-inferred truths for the intrinsic CMB flux at 100 GHz are compared with the true values in each pixel. The top panels show the distributions of reconstruction errors per pixel for the two methods, along with the widths of the best-fitting Gaussians for these distributions. Comparing the raw data (i.e. including SZ clusters, convolution with the beam and noise) with the true intrinsic CMB pixel values, leads to a best-fitting Gaussian width of 1.70 mJy, so it is apparent that both pixon and ML reconstructions have cleaned the data to some extent, although the narrowing of the error distribution is significantly better for the pixon case. The lower panels show trends for both the mean (solid lines) and standard deviation (dotted lines) of the flux errors as a function of the true pixel flux. In the ML case, the scatter in the flux errors is large and approximately independent of the true signal, whereas for the pixon reconstruction the scatter is suppressed but increases when the signal is strong and the pixon width being used becomes smaller. Where the scatter in the error increases, the mean difference between the pixon-inferred and true signals decreases. This shows that for pixels with absolute values of intrinsic CMB 100 GHz flux exceeding ~ 6 mJy, a smaller pixon width has been selected and the fit has improved. The choice of pixon widths is thus very important in determining these results. In the ML case, the trend in the mean error shows that the peak sizes are systematically underestimated.

Figure 3 is a greyscale comparison of the true (top panel), ML-inferred (middle) and pixon-inferred (bottom) cluster y maps. It is apparent that the pixon reconstruction has greatly suppressed the noise relative to the ML effort. There are a few sources in the pixon reconstruction that do not correspond with single identifiable sources in the actual truth. In regions where the density of small clusters is particularly high, the pixon algorithm has a tendency to place a single bright source to model the emission. However, relative to the ML effort, the compression of the reconstructed information is very clear. The pixon algorithm has essentially already made the decision as to which of the many ML sources are statistically justifiable. The mean Compton y parameters per pixel in units of 10^{-6} are 0.80, 1.25 and 0.79 for the true, ML and pixon images respectively, so the pixon algorithm does a good job of conserving the entire thermal SZ flux, in contrast to the ML technique.

As an aside, the inclusion of an intrinsic CMB component does not affect the cluster detection efficiency significantly. The important quantity is the signal-to-noise ratio with which the clusters alone would be observed. Other foregrounds such as dust and Galactic free-free and synchrotron emissions

are unlikely to vary on small scales and should not greatly affect the ability of the algorithm to detect clusters (see e.g. [11]).

3 Conclusions

The application of a speedy pixon method to some simulated Planck data has been described. This shows the ability of the technique to detect sources in low signal-to-noise data without introducing spurious objects. These results are a marked improvement over a simple maximum likelihood reconstruction procedure which is applied in the data pixel grid and includes a uniform image prior term. The speedy pixon algorithm is such that the treatment of 512^2 pixel images is possible using only ~ 20 minutes on a typical workstation.

ACKNOWLEDGMENTS

I would like to thank Rüdiger Kneissl for providing the CMB map. This work was carried out with the support of a PPARC postdoctoral fellowship.

References

1. Piña R.K., Puetter R.C., 1993, *PASP*, 105, 630 (PP93)
2. Smith C.H., Aitken D.K., Moore T.J.T., Roche P.F., Puetter R.C., Piña R.K., 1995, *MNRAS*, 273, 354
3. Metcalf T.R., Hudson H.S., Kosugi T., Puetter R.C., Piña R.K., 1996, *ApJ*, 466, 585
4. Dixon D.D. et al., 1996, *A&AS*, 120, 683
5. Dixon D.D. et al., 1997, *ApJ*, 484, 891
6. Knödlseeder J. et al., 1996, *SPIE Vol. 2806*, 386
7. Puetter R.C., 1996, *Proc. SPIE Vol. 2827*, 12
8. Eke V.R., 2000, *MNRAS*, submitted (astro-ph/9912078)
9. Tauber J., Pace O., Volonté S., 1994, *ESAJ*, 18, 239
10. Sunyaev R.A., Zel'dovich Ya. B., 1972, *Comm. Astrophys. Space Phys.*, 4, 173
11. Hobson M.P., Jones A.W., Lasenby A.N., Bouchet F.R., 1998, *MNRAS*, 300, 1
12. Seljak U., Zaldarriaga M., 1996, *ApJ*, 469, 437
13. Eke V.R., Navarro J.F., Frenk C.S., 1998, *ApJ*, 503, 569
14. Press W.H., Schechter P., 1974, *ApJ*, 187, 425